2016

Polarimetric Radar Observations of Precipitation Type and Rate from the 2–3 March 2014 Winter Storm in Oklahoma and Arkansas

Matthew S. Van Den Broeke

Dana M. Tobin

Matthew R. Kumjian

Polarimetric Radar Observations of Precipitation Type and Rate from the 2–3 March 2014 Winter Storm in Oklahoma and Arkansas

MATTHEW S. VAN DEN BROEKE

Department of Earth and Atmospheric Sciences, University of Nebraska—Lincoln, Lincoln, Nebraska

DANA M. TOBIN AND MATTHEW R. KUMJIAN

Department of Meteorology and Atmospheric Science, The Pennsylvania State University, University Park, Pennsylvania

(Manuscript received 6 January 2016, in final form 22 April 2016)

ABSTRACT

A powerful winter storm affected the south-central United States in early March 2014, accompanied by elevated convective cells with hail and high rates of sleet, freezing rain, and snow. During portions of the event the thermal profile exhibited a shallow surface cold layer and warm, unstable air aloft. Precipitation falling into the cold layer refroze into ice pellets and was accompanied by a polarimetric refreezing signature and numerous crowdsourced surface ice pellet reports. Quasi-vertical profiles of the polarimetric variables indicated an enhanced reflectivity factor Z_{HH} below the melting layer bright band and enhanced low-level differential reflectivity Z_{DR} values coincident with surface ice pellet reports. Freezing rain rate was highest in areas with high Z_{HH} and specific differential phase K_{DP} values at low levels. High snow rates were most closely associated with 1- and 1.5-km Z_{HH} values, though K_{DP} and Z_{DR} also appeared to show some ability to distinguish high snow rate. Numerous elevated convective cells contained rotating updrafts that appeared to contribute to storm longevity and intensity. Most contained well-defined Z_{DR} maxima or columns and relatively high base-scan Z_{DR} values. Several contained polarimetric signatures consistent with heavy mixed-phase precipitation and hail; social media reports indicated that large hail was produced by some of the storms.

1. Introduction

A powerful winter storm affected the southern United States on 2–3 March 2014, bringing substantial snow, sleet (hereafter ice pellets), and freezing rain accumulations to a large region spanning from Oklahoma eastward to Maryland, Delaware, and southern New Jersey. Early in the event, a strong Arctic cold front advanced south across Oklahoma and Arkansas, with warm, unstable air above the frontal surface. This resulted in heavy snow, ice pellets, and freezing rain accumulations, with embedded thunderstorms (e.g., NWS 2014a,b). Lengthy power outages and substantial transportation impacts resulted. The event also was associated with a well-defined polarimetric refreezing signature (Kumjian et al. 2013; Kumjian and Schenkman 2014) and offers a good opportunity to study precipitation rate and elevated convective signatures in a winter storm environment.

Freezing rain is common to the north of a surface Arctic cold front, where a shallow cold air mass near the surface is overlain by much warmer air aloft (e.g., Prater and Borho 1992; Rauber et al. 2001). When synoptic-scale or mesoscale forcing is sufficient for precipitation, ice pellets may be produced as initially frozen hydrometeors fully or partly melt within a layer of air aloft with wet-bulb temperatures > 0°C and subsequently refreeze within a subfreezing layer below (e.g., Hanesiak and Stewart 1995; Zerr 1997). The particle refreezing rate is slower for larger particles and if the cold layer is barely subfreezing (Zerr 1997). Simulations by Zerr (1997) indicate a large depth of cold air is required for large concentrations of drops to completely refreeze, possibly resulting in mixed-phase precipitation reaching the surface if the cold layer is shallow or weak. These particles may be reported as ice pellets or freezing rain depending on the particle's ice fraction (Zerr 1997), or as a mixture of precipitation types (e.g., Elmore et al.

Corresponding author address: Matthew S. Van Den Broeke, 306 Bessey Hall, Lincoln, NE 68588-0340.
E-mail: mvandenbroeke2@unl.edu

DOI: 10.1175/WAF-D-16-0011.1

2014). Refreezing layers (RFLs) have been associated with a unique polarimetric signature (Kumjian et al. 2013), distinct from the one associated with the melting layer bright band near the 0°C level (e.g., Austin and Bemis 1950; Zrnić et al. 1994; Giangrande et al. 2008). RFLs are characterized by enhanced differential reflectivity Z_{DR} and specific differential phase K_{DP} values and decreased copolar correlation coefficient ρ_{hv} values within decreasing values of the reflectivity factor Z_{HH} (Kumjian et al. 2013). Though not fully understood at this time, the most plausible explanation for the observed refreezing signature is the preferential freezing of small liquid drops. This reduction in their dielectric constant reduces their contribution to Z_{HH}, leading to higher Z_{DR} values as the power return is dominated by larger mean drop sizes. Slightly reduced fall speed during freezing results in a slight increase in K_{DP} values, and increased wobbling and a mixture of particles in various stages of freezing decrease ρ_{hv} (Kumjian et al. 2013).

Precipitation rate in winter storms is a function of precipitation type (e.g., Thériault et al. 2006). Larger snowflakes are typically associated with higher precipitation rates and, upon encountering a warm layer, may melt partially and refreeze into ice pellets, whereas small snowflakes or pristine crystals may melt completely and arrive at the surface as freezing rain (Thériault et al. 2010). Winter precipitation rates have been estimated on the scale of entire winter storms (Thorp and Scott 1982), as well as daily and hourly rates (e.g., Rudolph et al. 2011). Radar observations have been used to estimate the precipitation rate, with increasing correspondence found for gauge observations closer to the radar site (e.g., Joss and Lee 1995). Reflectivity values tend to be roughly equal in ice- or liquid-phase precipitation for constant liquid-equivalent precipitation rate (Marshall and Gunn 1952).

Several prior studies have focused on polarimetric radar features in winter storms and their relationship to surface precipitation rates. Kennedy and Rutledge (2011) showed that, in Colorado winter storms, the surface precipitation rate may increase substantially as bands of enhanced K_{DP} near the ambient −15°C level move overhead; these are thought to represent zones of rapid dendritic growth and subsequent aggregation. In some cases, these K_{DP} signatures are associated with enhanced Z_{DR} and reduced ρ_{hv} (e.g., Andrić et al. 2013; Schrom et al. 2015), indicating anisotropic crystals dominate the backscatter. Similar K_{DP} enhancements have been identified in other Colorado winter storms (Schrom et al. 2015), in Oklahoma (Andrić et al. 2013), across the Swiss Alps (Schneebeli et al. 2013), in Italy (Bechini et al. 2013), over the northeastern United States (Griffin et al. 2014), and in Finland (Moisseev et al. 2015). Oftentimes, the rapid depositional growth aloft leads to large aggregates and high snowfall rates near the surface associated with large Z_{HH} values (e.g., Griffin et al. 2014).

Precipitation type and rate in winter storms may also be strongly influenced by the presence of elevated convection. Strong warm-air and moisture advection have been noted in an elevated layer during similar past events (e.g., Holle and Watson 1996). Elevated convection may often be marked by high Z_{HH} and relatively low Z_{DR}, possibly as a result of more isotropic graupel particles (Hogan et al. 2002). Other studies, however, have found elevated convection to be associated with pockets of relatively high Z_{DR} values (e.g., Andrić et al. 2013), or turrets of near-zero Z_{DR} enshrouded by large Z_{DR} values (Kumjian et al. 2014). Elevated convection within winter storms has been observed to produce lightning [primarily in-cloud flashes, e.g., Rauber et al. (1994); Trapp et al. (2001); Kumjian and Deierling (2015)]. Lightning-producing elevated convection may be associated with enhanced K_{DP} values, and areas near lightning flashes are often characterized by relatively high Z_{HH} and low Z_{DR}, consistent with graupel (Kumjian and Deierling 2015). It may be associated with high precipitation rates below prolific ice crystal generation or riming aloft (Trapp et al. 2001; Crowe et al. 2006), sometimes associated with cloud-top reflectivity maxima in generating cells (e.g., Plummer et al. 2014; Rosenow et al. 2014; Keeler et al. 2016), and may preferentially occur in regions of reduced static stability (Doswell 1990). Given a sufficient thermodynamic profile, heavy freezing rain may also result from elevated convection (e.g., Rauber et al. 1994). Elevated wintertime convection may be most common when an Arctic front is nearby with strong southwest flow aloft (Hunter et al. 2001), though it may also be associated with warm fronts (Rauber et al. 1994). In the presence of adequate vertical wind shear, supercell convection has been observed to be rooted in the boundary layer north of an Arctic front within a subfreezing air mass (Trapp et al. 2001).

In most prior studies, the focus of using polarimetric radar variables in winter storm environments has been to describe signatures associated with specific precipitation types and microphysical processes. Less attention has been given to precipitation rate and impacts at the surface in winter storms. Thus, using a polarimetric dataset collected during a winter storm in Oklahoma and Arkansas, this study provides preliminary observations of the following:

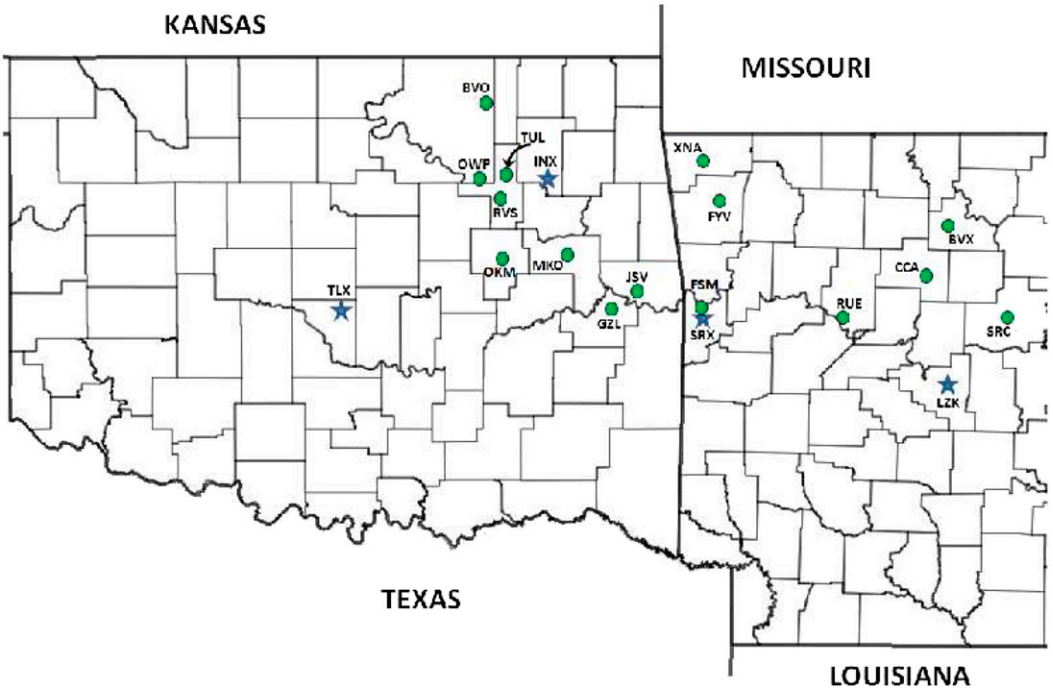

FIG. 1. ASOS stations (green circles) used for precipitation rate calculations, and radar sites (blue stars) used in the polarimetric radar analysis. OK and AR counties are outlined.

1) relationships between the polarimetric refreezing signature and crowdsourced surface precipitation reports;
2) associations between the rates of freezing rain/snow and polarimetric radar characteristics; and
3) polarimetric signatures of elevated convection, including elevated storms with rotating updrafts, during the winter storm event.

These observations and analyses will be helpful to the operational and research communities in future work nowcasting severe winter weather impacts (i.e., surface precipitation type and amount) and understanding winter storm microphysics.

2. Data and methods

The analysis of dual-polarized radar datasets herein includes data from four Weather Surveillance Radar-1988 Doppler (WSR-88D) stations in Oklahoma and Arkansas. Data were included across the time when winter precipitation was falling in each radar's domain. These WSR-88D locations include (Fig. 1)

1) Fort Smith, Arkansas (KSRX), from 1300 UTC 2 March to 0300 UTC 3 March 2014;
2) Little Rock, Arkansas (KLZK), from 1300 UTC 2 March to 0400 UTC 3 March 2014;
3) Tulsa, Oklahoma (KINX), from 1500 UTC 2 March to 0800 UTC 3 March 2014; and
4) Twin Lakes, Oklahoma (KTLX) from 1600 UTC 2 March to 0000 UTC 3 March 2014.

The first three sites were used in analyses of the precipitation rate, while KTLX was used primarily for analysis of the polarimetric refreezing signature. Polarimetric variables utilized in the analysis for these radars were Z_{DR}, ρ_{hv}, and K_{DP} [for more information on these variables, see Zrnić and Ryzhkov (1999), Bringi and Chandrasekar (2001), Ryzhkov et al. (2005), and Kumjian (2013a–c)]. All altitudes noted throughout the paper are above radar level (ARL).

Automated Surface Observing System (ASOS) stations in the domain of the four radars listed above were located. Though these stations typically report weather conditions on an hourly basis, observations of higher temporal resolution are available from some stations; these stations are more useful for diagnosing the precipitation rate in this winter storm because the precipitation rate often fluctuated markedly over short time periods. Liquid equivalent precipitation accumulation is available from most ASOS stations, reported as a value since the prior hourly observation. Thus, it is occasionally possible to obtain a liquid equivalent precipitation rate for relatively short time periods. Precipitation rate was calculated for time periods meeting the following criteria.

1) The time period was ≤20 min in length. In this winter storm, precipitation was commonly organized into areas of higher precipitation rate and convection, with areas of lighter precipitation between. Thus, a longer time period would have not accounted for the unsteady nature of the precipitation rate during this event. A 20-min threshold allowed for radar variable values from three to four sample volumes to be averaged, increasing the robustness of the results. When such averaging was not possible (e.g., for analysis periods only encompassing one or two sample volumes), it was verified that precipitation rate was nearly constant throughout the analysis period. Thus, all analysis periods were chosen such that precipitation was mostly steady throughout. Five-minute ASOS data were not employed primarily because they were only available for 8 of the 15 ASOS stations selected.
2) The precipitation rate was nonzero.
3) Precipitation type was reported as either snow or freezing rain. Although periods were reported with mixed precipitation types, they were not numerous enough to produce robust statistics, and also were associated with larger error when an advection correction was applied (described below).

Precipitation rate data from 15 ASOS stations (Fig. 1) were included to calculate the statistics described herein. Not all of these stations utilize the same type of precipitation sensor. Most use the older, heated tipping-bucket gauges, while the stations at Tulsa, Oklahoma (KTUL), and Fort Smith, Arkansas (KFSM), utilize all-weather precipitation accumulation gauges (AWPAG). These sensor differences are associated with some variability in precipitation collection efficiency, and therefore estimated precipitation rate, especially in snowfall. Good discussion of these sensors, as well as sources of errors typically associated with wintertime precipitation measurement by ASOS, is presented in Rasmussen et al. (2012) and Martinaitis et al. (2015). In snow, typical errors are on the order of 20%–50% (Thériault et al. 2012; Rasmussen et al. 2012), indicating that substantial error could be introduced to precipitation rate estimates using ASOS. These errors are difficult to quantify, given the lack of ground-truth estimates of precipitation rate, especially on short time scales. This, in turn, renders especially preliminary the findings of how polarimetric variables are related to snow rates.

For the time periods used to calculate the precipitation rate, radar sample volumes falling within this time period were used to estimate mean values of Z_{HH}, Z_{DR}, ρ_{hv}, and K_{DP} over the ASOS site, corrected for hydrometeor advection, during the period of interest for each elevation angle at or below the ambient 700-hPa level. Advection correction consisted of the following procedure:

1) identify the altitude of the beam centerline over each ASOS station (km);
2) associate a typical terminal velocity with the type of precipitation reported, using the following values:
   (i) freezing rain—for a 2-mm liquid drop, typical terminal velocity is ~650 cm s^{-1} (e.g., Gunn and Kinzer 1949; Gossard et al. 1992);
   (ii) snow aggregates—for an 8-mm aggregate falling at −5°C, typical fall velocity is ~110 cm s^{-1} (Brandes et al. 2008);
   note that substantial error may be introduced if the mean particle sizes were substantially different than assumed here;
3) calculate the total time for a particle to fall from beam centerline to the surface;
4) calculate the mean wind speed and direction in the below-beam-centerline layer from representative model sounding(s); and
5) determine the distance and direction of particle advection during the fall time, and define a new advection-corrected location most representative of where precipitation that reached the surface at the ASOS station would have fallen through the radar beam.

Mean values were calculated by identifying the pixel at the advection-corrected location, recording the value of a given variable at this and the eight surrounding pixels (nine contiguous pixels), repeating this for each sample volume during the analysis period, and averaging the values for all pixels. As a hypothetical example, a 15-min analysis period might contain three sample volumes, each with nine pixel values of each variable, so the final average value would consist of an average value of all 27 pixels. Averages were not calculated for ρ_{hv} or K_{DP} if the ρ_{hv} value was >1 (often indicating low signal-to-noise ratio). Polarimetric averages were also related to the approximate temperature of the beam centerline, estimated using the nearest archived Rapid Refresh (RAP) model sounding at the time nearest the radar observations. For ASOS sites not spatially close to an archived RAP sounding, an average of surrounding sites was used. For example, the temperature aloft at Stigler, Oklahoma (KGZL; Fig. 1), was estimated as an average of the values at McAlester, Oklahoma (KMLC), and at KFSM.

Radar observations also were supplemented by surface precipitation reports using data from the mobile Precipitation Identification Near the Ground (mPING) mobile device app, contributed to by a broad network of citizen scientists and described by Elmore et al. (2014). These precipitation reports are anonymously submitted by the public from mobile devices equipped with GPS

tracking capabilities and are freely available online (mping.nssl.noaa.gov/display). Information about the project may also be found at the NSSL website (www.nssl.noaa.gov/projects/ping) and in Elmore et al. (2014). These mPING observations provide high spatial and temporal resolution surface precipitation type reports, and have been utilized in prior winter weather studies (e.g., Griffin et al. 2014; Picca et al. 2014; Kumjian and Schenkman 2014; Elmore et al. 2015; Chen et al. 2016). Radar analyses were also supplemented by routine upper-air observations, in addition to archived RAP model output at times and locations representative of the environments near the selected ASOS stations (Fig. 1). These data were used to estimate the vertical temperature and wind profiles associated with radar sample volumes.

Finally, analysis of a long-duration polarimetric refreezing signature present during this case includes quasi-vertical profiles (QVPs) of the polarimetric radar variables (e.g., Kumjian et al. 2013; Ryzhkov et al. 2016) in conjunction with mPING reports. For every range gate at a particular elevation angle, QVPs are constructed by averaging over all azimuths to produce a polarimetric radar variable profile representative of a region around the radar. Profiles for higher elevation angles most accurately represent the atmosphere within a small region around the radar. The 2.4°-elevation angle, however, was used for computing QVPs in ice pellet cases because the refreezing signature is at low levels and appears to be captured well at this elevation. It is important to note that the QVPs average over an increasingly large area around the radar at higher altitudes and may not be representative of smaller-scale features within the region of interest.

Precipitation reports from mPING within a 100 km × 100 km grid centered on the radar were used to accompany the QVPs and provide surface hydrometeor types, which may help to determine the hydrometeors responsible for producing the observed radar profiles. This analysis assumes the near homogeneity of precipitation within the grid. Localized precipitation reports may be representative of polarimetric signatures that are smoothed out during averaging. If multiple precipitation types are reported simultaneously within the domain, it may be indicative of either multiple precipitation types at the same location, or evidence of a transition or precipitation type boundary within the domain.

3. Environmental overview

The synoptic situation leading to this winter precipitation event was similar to scenarios described in the literature (e.g., Bernstein 2000; Robbins and Cortinas 2002). An upper-level trough approached the California coast on 28 February 2014, with an Arctic high pressure system over the northern Great Plains (not shown). This trough crossed the Rockies with its axis located from eastern Utah through eastern Arizona by 1200 UTC 2 March 2014 (Fig. 2a). Heavy winter precipitation was ongoing across Oklahoma and Texas at this time. Oklahoma and Arkansas were also in the right-entrance region of a departing 300-hPa jet streak, favoring upper-level divergence (Fig. 2a). Ahead of the trough, broad southwesterly 700-hPa flow was located from Texas to Oklahoma and Arkansas (Fig. 2b). Nearer the surface, a surge of Arctic air was progressing southward (Fig. 2c). The 850-hPa temperatures were generally >10°C over Texas and Arkansas in southwesterly flow, with a strong temperature gradient northward and temperatures from −10° to −15°C over Kansas (Fig. 2c). At the surface, the Arctic front was surging across Oklahoma, with temperatures 10°–18°C over northeast Texas and southwest Arkansas, decreasing to near −18°C in northern Kansas (Fig. 2d). Moist air was present south of the frontal boundary, with dewpoint temperatures near 16°C over northeast Texas and southwest Arkansas. Dewpoint depression values were generally small north of the front (Fig. 2d).

Early in the event, the cold air layer was shallow and supportive of freezing rain. For example, the 2000 UTC RAP sounding from KFSM has a subfreezing layer < 1 km in depth, with temperature and dewpoint near 10°C in the warm layer aloft (Fig. 3a). Elevated instability was also present, with 195 J kg^{-1} of most unstable convective available potential energy (MUCAPE) present in the 3–8-km layer (yellow line in Fig. 3a shows the path of a parcel lifted from 2 km, producing this MUCAPE value). In addition to the instability, 23 m s^{-1} of vector wind difference, 173 m^2 s^{-2} of helicity, and a veering vertical wind profile were present in the 2–8-km layer, indicating an environment favorable for elevated severe convection. Some thunderstorms forming in this elevated convection-favorable environment produced large hail (e.g., Fig. 3c). The shallow cold layer above the surface rapidly deepened through 2 March 2014, allowing precipitation to transition from freezing rain to ice pellets. Figure 3b shows the KFSM sounding from 0000 UTC 3 March 2014, in which the subfreezing layer had strengthened and deepened by nearly 0.5 km compared to 4 h earlier. Warm, humid air aloft remained supportive of elevated convection through 0000 UTC on 3 March (Fig. 3b), though the MUCAPE value by this time had decreased to 80 J kg^{-1}. Thus, throughout the duration of this event the environment was supportive of elevated convection and wintry precipitation at the surface, including a long episode of ice pellets described in the next section.

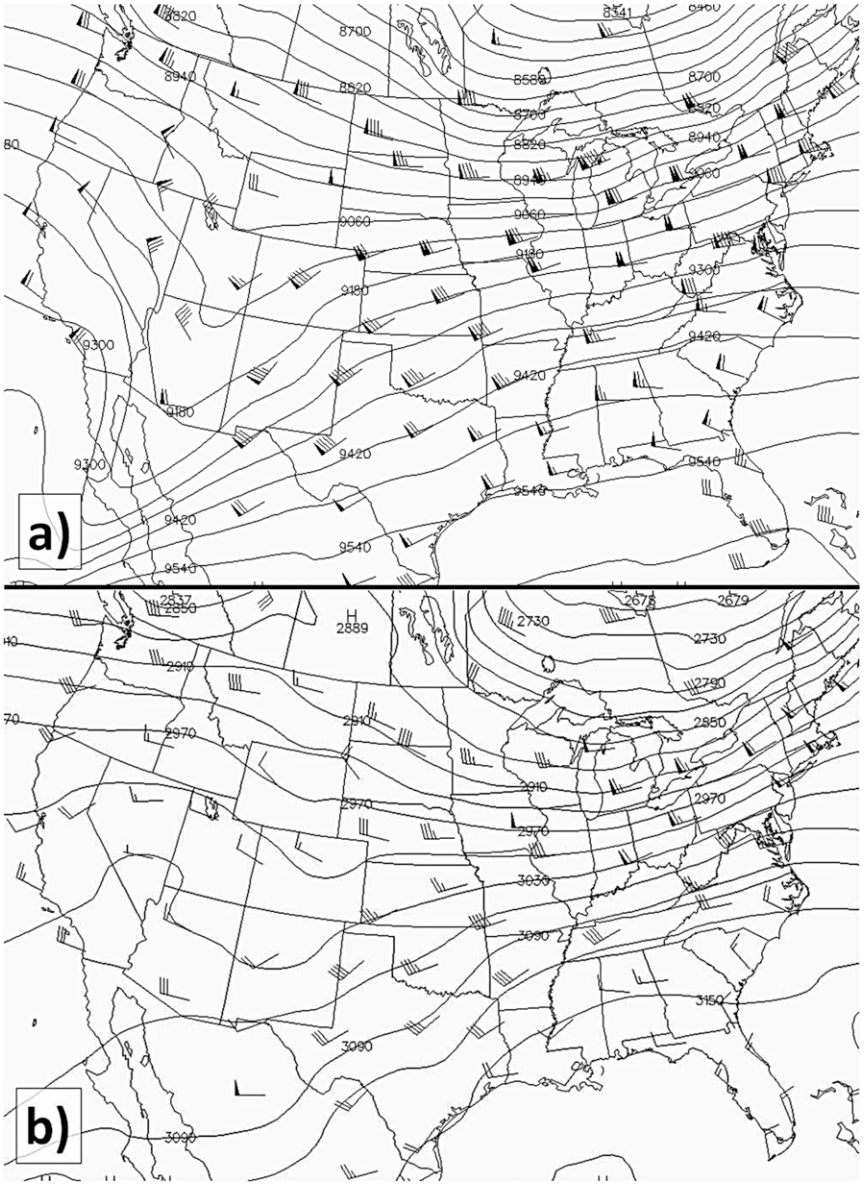

FIG. 2. Observations from 1200 UTC 2 Mar 2014: (a) 300-hPa geopotential height (contoured every 60 m) and wind barbs (half-barb = 5 kt, where 1 kt = 0.51 m s^{-1}; full barb = 10 kt; and flag = 50 kt); (b) 700-hPa geopotential height (contoured every 30 m) and wind barbs as in (a); (c) 850-hPa temperature (contoured every 5°C) and wind barbs as in (a); (d) surface observations, with station plot temperature (red) in °C, wind barbs (kt) as in (a), surface pressure contoured every 4 hPa, and dewpoint (°C) color shaded according to the scale on the right. [Data in (a)–(c) generated at The Plymouth State Weather Center; observations in (d) plotted using WeatherScope software from the Oklahoma Climatological Survey.]

4. Polarimetric refreezing signature related to surface precipitation reports

Given an environment supportive of freezing rain and ice pellets for a prolonged period, it is no surprise that a persistent polarimetric hydrometeor refreezing signature was observed with KTLX throughout much of 2 March 2014. Similar to results reported in Kumjian et al. (2013), the signature is characterized by an enhancement in Z_{DR} within a region of decreasing Z_{HH} and ρ_{hv}. Coincident with the signature were numerous crowdsourced mPING reports of ice pellets across central Oklahoma.

To capture the evolution of the vertical precipitation structure, QVPs were computed between 1600 and 0000 UTC (Fig. 4). At the beginning of this report period,

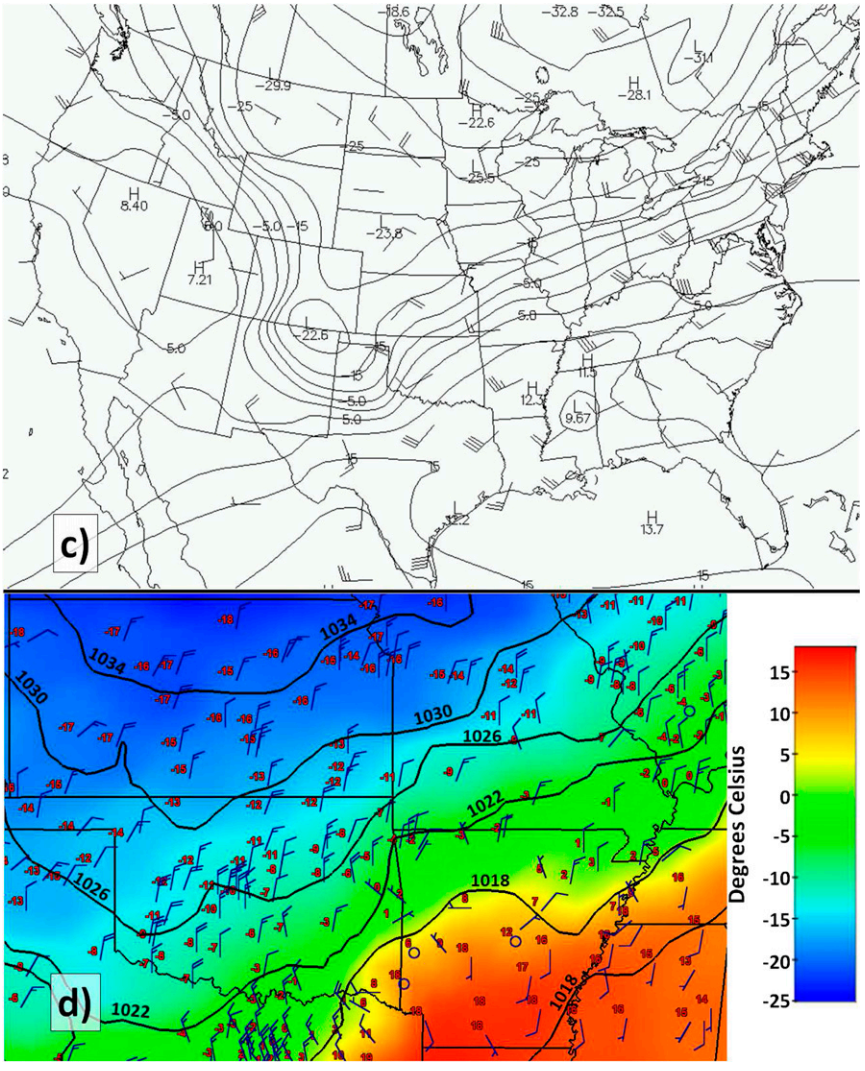

FIG. 2. (*Continued*)

mPING reports indicated snow at the surface, and there was no polarimetric refreezing signature present. In fact, the QVPs reveal light Z_{HH} echoes associated with large positive Z_{DR} in the shallow near-surface cold layer. Based on RAP-analyzed temperatures (Fig. 3), these signatures are consistent with locally generated columnar ice crystals. Between 1700 and 1730 UTC, the QVPs suggest stronger, deeper echoes and a more pronounced melting layer, suggesting precipitation generation over a deeper layer, melting, and hydrometeors falling into the near-surface cold layer. The first ice pellet (IP) reports in the domain around KTLX were made at 1712 UTC.

From 1743 to 1928 UTC, dozens of reports were made of IP, snow (SN), and ice pellets mixed with snow (IP/SN). These mixed reports suggest the low-level columnar ice crystals and ice pellets continued to reach the surface. Polarimetric profiles starting at 1815 UTC generally show a well-defined refreezing signature below 1 km ARL in Z_{DR}. However, a small ''break'' in the refreezing signature (gap in the low-level Z_{DR} enhancement) between 1850 and 1907 UTC occurs and appears to match a notable lack of IP reports. This period corresponds with reduced Z_{HH} values ($<$10 dBZ), likely indicating a brief period of lighter precipitation, which would account for the reduced number of mPING reports at this time. After 1907 UTC, the enhancement in Z_{DR} resumed, and IP dominated the precipitation reports with slightly fewer reports of SN. Lighter, more scattered precipitation is found over the domain after 2130 UTC, and subsequently the signatures become less pronounced until about 2300 UTC. After that, the QVPs are reminiscent of the earlier snow period, and indeed SN dominates the mPING

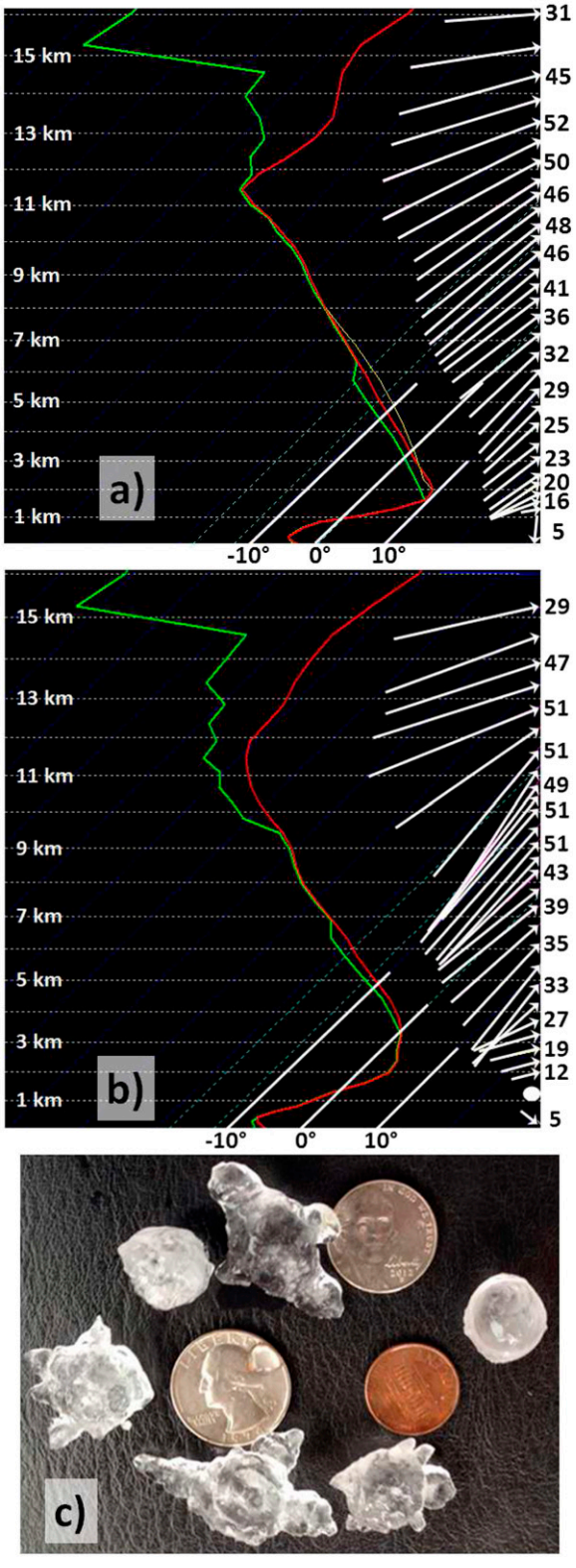

FIG. 3. RAP soundings from KFSM at (a) 2000 UTC 2 Mar and (b) 0000 UTC 3 Mar 2014. Wind speeds indicated to the right of the sounding ($m\,s^{-1}$). (c) An example of large hail collected in central OK after passage of an elevated convective cell at ~2227 UTC. (Courtesy E. Davidson.)

reports with only isolated IP reports made after this time (not shown).

A time period with consistent IP reports and a relative lack of other precipitation-type reports from 1937 to 2039 UTC was chosen to characterize the refreezing signature. QVPs during this time show persistent characteristics with only moderate scan-to-scan variability (Fig. 5). A total of 72 IP, 25 IP/SN, and 2 SN reports were submitted during this time frame within the domain around KTLX. Seven hail (HA) reports were also submitted. Some of these reports may be erroneous (i.e., citizens incorrectly identified IP as HA; however, large (>2.5 cm) hail accompanied by thunder and lightning was reported on social media around 2000 UTC (e.g., Fig. 3c). Thus, some of the HA reports may be valid. Similar mixtures of HA and IP have occurred in convective winter storms in this region (e.g., Kumjian et al. 2013).

Average QVPs for this time period are plotted in Fig. 5. There is a pronounced Z_{HH} maximum between 0.5 and 1.0 km, located beneath the melting-layer bright band (itself centered near 2.5 km) and in a region of temperatures < 0°C according to the 2000 UTC RAP Oklahoma City, Oklahoma (KOKC), sounding (not shown). A similar enhancement was described but not discussed in Kumjian et al. (2013). Just above the Z_{HH} maximum, where Z_{HH} values begin to increase rapidly with decreasing height (near 1 km), Z_{DR} remains constant. This implies hydrometeors increasing in size and/or concentration without preference to a particular part of the size spectrum and without significant changes in the dielectric constant, possibly consistent with a decrease in hydrometeor fall speeds at the very onset of refreezing. A pronounced enhancement in Z_{DR} is found at 0.6 km, with peak values near 1.0 dB, located about 100 m beneath the Z_{HH} maximum in a region where Z_{HH} decreases toward the ground. The Z_{DR} enhancement is collocated with the beginning of a ρ_{hv} reduction. These signatures are consistent with the hypothesis of preferential refreezing of the smallest drops. Beneath that, ρ_{hv} precipitously decreases toward the surface as ground clutter starts to contaminate the signal. These signatures indicate complex microphysical processes occurring within the refreezing layer. Future work involving more observations, microphysical modeling, and in situ observations likely will help us to better understand these processes.

5. Preliminary comparisons of precipitation rate and polarimetric radar observations

Precipitation type reported by ASOS was divided into freezing rain (FZRA; 49 analysis periods) and SN

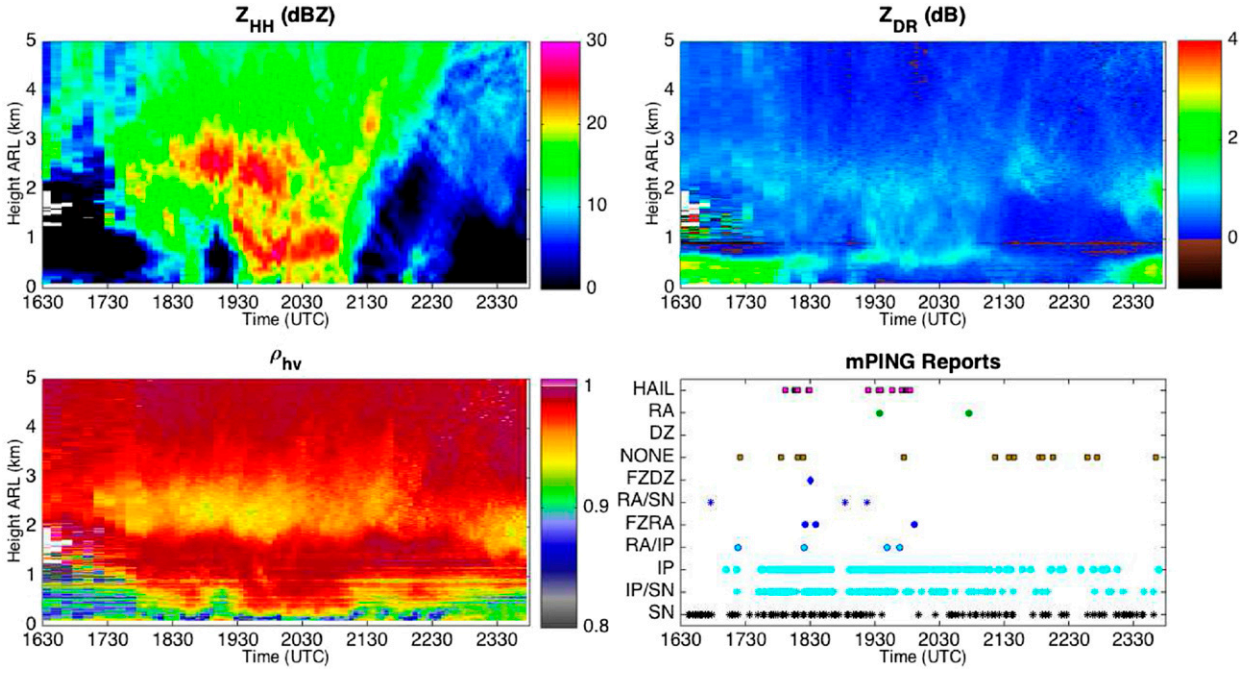

FIG. 4. QVPs of Z_{HH}, Z_{DR}, and ρ_{hv} (UTC) with accompanying mPING precipitation reports. In the mPING reports, HAIL (magenta squares) are hail, RA (green circles) are rain, NONE (brown squares) are reports of no precipitation, FZDZ (blue diamonds) are freezing drizzle, RA/SN (blue asterisks) are for rain/snow mixtures, FZRA (blue circles) are freezing rain, RA/IP (cyan circles with blue outline) are for rain/ice pellet mixtures, IP (cyan circles) are ice pellets, IP/SN (cyan asterisks) are ice pellet/snow mixtures, and SN (black asterisks) are snow reports.

(62 analysis periods). ASOS categorizations were compared to mPING precipitation types when available, usually with good agreement (e.g., as found by Elmore et al. 2014). Agreement was best with IP and IP/SN mixtures, perhaps because ASOS reports of IP require human intervention (e.g., Elmore 2011). Discrepancies between the two sources of precipitation-type information may arise from the high spatial variability of winter precipitation types (e.g., Schuur et al. 2012). Any study of winter precipitation type will be limited by these observational uncertainties; nevertheless, we feel the precipitation types assigned are sufficiently certain to allow for a robust preliminary analysis.

For each precipitation-type category, polarimetric signatures were investigated as a function of altitude and temperature of beam centerline (temperature estimated using RAP output; altitude assumes the standard 4/3 Earth radius model of beam propagation). Approximate altitudes examined were near cloud base (~1 km), near 850 hPa within the layer where the temperature was increasing rapidly with height (~1.5 km), and near 700 hPa, which was the approximate inversion top (~3 km). Analysis with respect to temperature produced generally stronger results, as expected given the strong inversion present in this case (e.g., Fig. 2). The K_{DP} value at −15°C was considered since it has been related to the surface snow rate (e.g., Kennedy and Rutledge 2011), though insufficient data points were available to allow a robust statistical analysis. In the results below, all correlation coefficients r are Pearson's correlations. All p values were calculated using a two-tailed Wilcoxon–Mann–Whitney (WMW) test, given the non-Gaussian nature of many of the distributions examined. All values of the radar variables discussed are the mean values over the time period for which the precipitation rate was calculated, over the nine pixels surrounding the advection-corrected observation site (as described in section 2).

a. Comparisons between freezing rain rate and the polarimetric variables

Correlation between FZRA rate and mean values of the polarimetric variables was stronger when the analysis was completed within a temperature-relative framework, though even in an altitude-relative analysis, higher FZRA rates were associated with higher mean values of cloud-base Z_{HH} and K_{DP} (not shown). This result is expected: higher Z_{HH} values are typically associated with higher rain rates, and higher K_{DP} values typically correspond to higher liquid water content

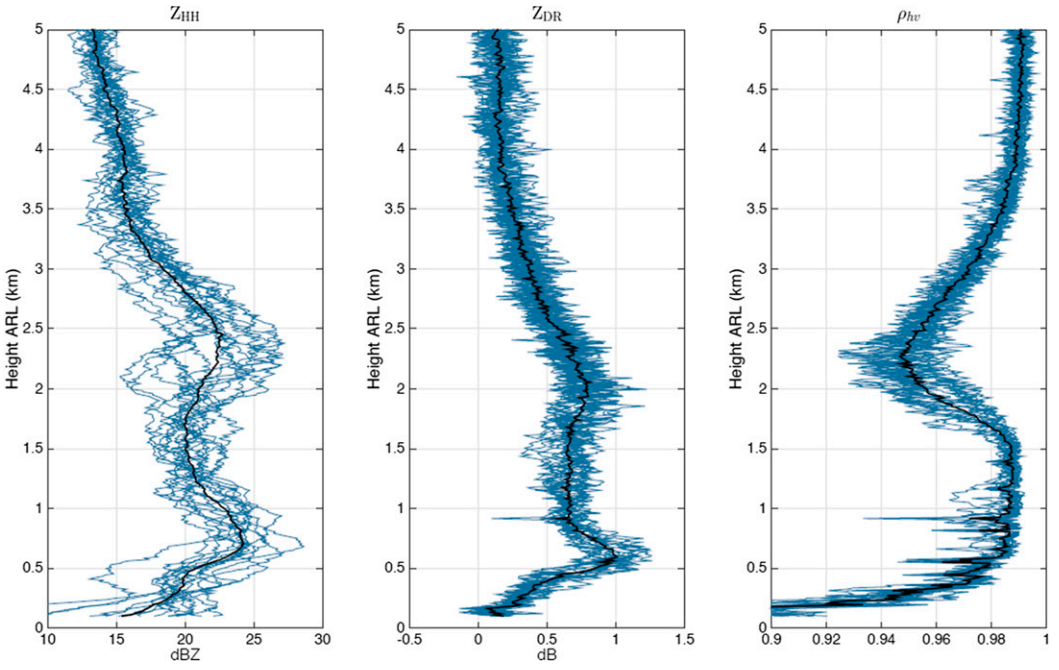

FIG. 5. QVPs from individual scans (blue) and the averaged QVPs (black) of Z_{HH}, Z_{DR}, and ρ_{hv} from 1937 to 2039 UTC.

(e.g., Bringi and Chandrasekar 2001). Mean 1-km Z_{HH} values were 10–25 dBZ for some low FZRA rates, and >25 dBZ during most of the highest FZRA rate analysis periods. FZRA rates of >3 mm h^{-1} were associated with mean 1-km K_{DP} values of >0.05° km^{-1}.

Among ~1-km data points, correlation values were moderate for all polarimetric variables except ρ_{hv} when the 1-km temperature was <0°C (Fig. 6). This relationship is strongest for Z_{DR} (Fig. 6b; $r = 0.64$) and K_{DP} (Fig. 6d; $r = 0.76$), which show a clear increasing trend with higher FZRA rate. At temperatures > 0°C at 1 km, associations were weak except for K_{DP}, which showed an increasing trend at higher FZRA rates ($r = 0.50$; not shown). Relationships between FZRA rate and the radar variables were generally not as strong at 1.5 and 3 km when segregated by temperature. One exception was at 1.5 km, where the correlation was moderate with Z_{HH} when the temperature was <+5°C ($r = 0.60$; Fig. 6e). This association is expected, as larger mean drop size should lead to higher Z_{HH} and precipitation rate. Correlations were generally low between the FZRA rate and mean values of the polarimetric variables near 700 hPa (3 km), possibly because of the complex thermal structure in this event, and possibly because of the mix of stratiform and deep convective precipitation.

The predictive ability of the highest FZRA rate values was sought among this dataset. These were defined as a FZRA rate of >5 mm h^{-1} (top ~22% of values). The population of high FZRA rate events was compared with the population of all other FZRA events, using a WMW test designed to test the likelihood of correspondence between two medians, at each of the three vertical levels examined (1, 1.5, and 3 km). First, temperatures between populations were compared to ensure sufficient similarity (e.g., to make sure that high FZRA rates were not associated with significantly warmer or colder conditions than the remainder of the events). For the 1- and 1.5-km levels, the temperature distributions were statistically similar ($p > 0.14$). At 1 km, the mean Z_{HH} value was 30.6 dBZ among high FZRA rate periods and 27.2 dBZ among other periods. At 1.5 km, mean Z_{HH} was 30.2 dBZ among high FZRA rate periods and 26.4 dBZ among other periods. These differences were not significant at $p < 0.05$, however. The K_{DP} mean values were also much higher for high FZRA periods (0.15° vs 0.06° km^{-1} at 1 km; 0.27° vs 0.05° km^{-1} at 1.5 km), though these differences also were not significant at $p < 0.05$. This suggests that Z_{HH} and K_{DP} may have the operational utility to distinguish high FZRA rates, though a larger dataset would be required to yield statistical significance.

b. *Comparisons between snow rate and the polarimetric variables*

Liquid equivalent precipitation rates were used in analysis periods dominated by SN ($n = 62$). Again,

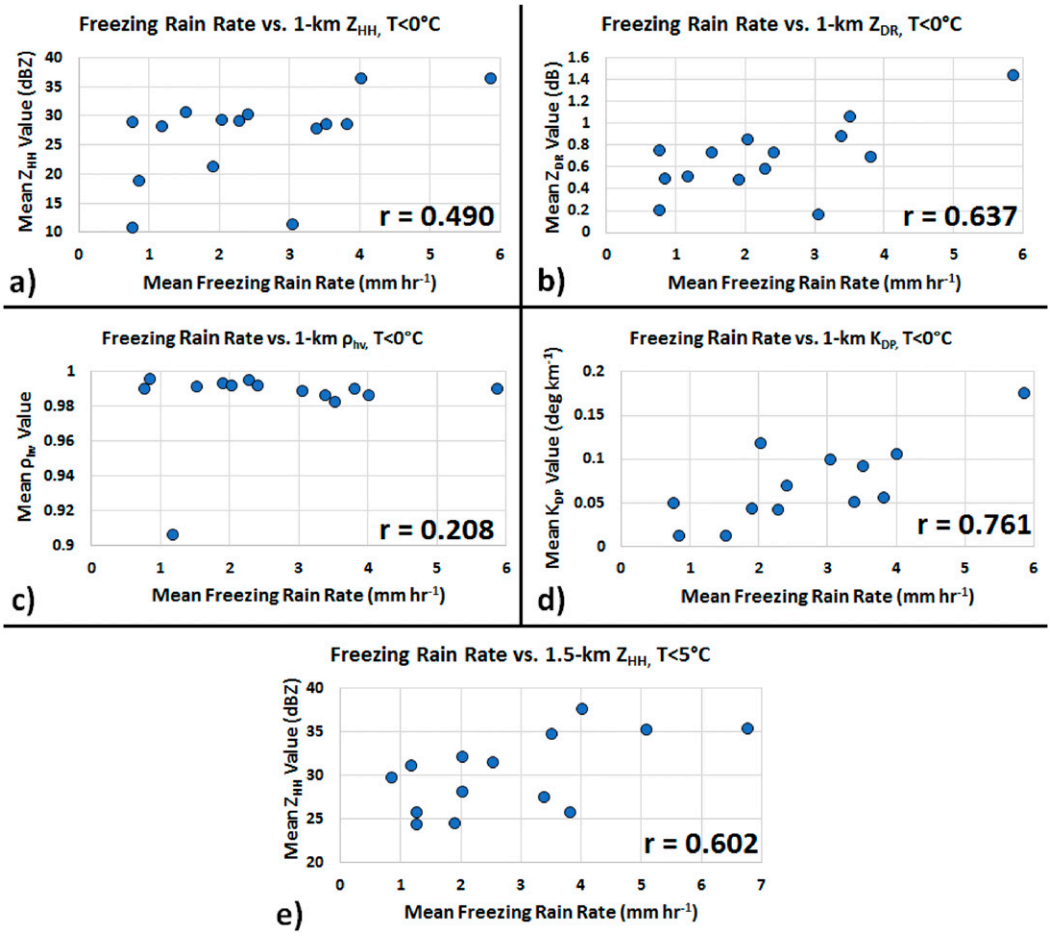

FIG. 6. Freezing rain rate vs mean values of the radar variables at the ~1-km level for all data points with temperature < 0°C: (a) Z_{HH}, (b) Z_{DR}, (c) ρ_{hv}, and (d) K_{DP}. (e) As in (a), but for all data points with temperature < 5°C at an altitude of ~1.5 km. Value of Pearson's correlation coefficient r is given in bottom right of each panel.

temperature-segregated data produced stronger associations between SN rate and mean values of the radar variables. When altitude segregated, Z_{HH} was best correlated to snow rate, with the strongest correlation at 1.5-km altitude ($r = 0.38$; not shown). Near cloud base (~1 km), correlations between SN rate and the polarimetric variables were highest at low temperatures (≤−5°C; Fig. 7). Higher SN rates were associated with relatively high Z_{HH} (Fig. 7a; $r = 0.46$) and Z_{DR} (Fig. 7b; $r = 0.57$), and with relatively low ρ_{hv} (Fig. 7c). These results were clearly biased by two analysis periods with exceptionally high SN rates (near 4 mm h^{-1}; Fig. 7); the combination of polarimetric variables in these events suggests the presence of wet snow and thus RAP model analysis temperature errors (e.g., Griffin et al. 2014). A larger sample of events spanning a wider distribution of SN rates may provide additional insight. Similar associations occurred among the 1-km data when the temperature was >−5°C, but the correlation values were not as high. Associations were generally similar between the surface SN rate and the polarimetric variables at 1.5 and 3 km. High Z_{HH} and K_{DP} values were associated with increased SN rates; for example, K_{DP} was moderately correlated with SN rate at 1.5-km altitude when that level was warmer than 0°C (Fig. 7d).

Radar variables were again sought that were most predictive of high SN rates. For the top 29% of SN rates (rate > 2.25 mm h^{-1}; $n = 18$), the temperature distribution was statistically similar at the 1- and 1.5-km levels ($p > 0.05$), allowing comparison of mean values of the polarimetric variables there. The 1-km mean Z_{HH} was 28.1 dBZ among high SN rate periods and 22.8 dBZ among other SN periods. The 1.5-km Z_{HH} was also much higher for high SN rates (36.4 vs 22.4 dBZ), but these results were not statistically different between the two populations. In addition, Z_{DR} values were higher among high SN rate periods at 1 and 1.5 km, and K_{DP} values at 1.5 km were substantially higher (but not

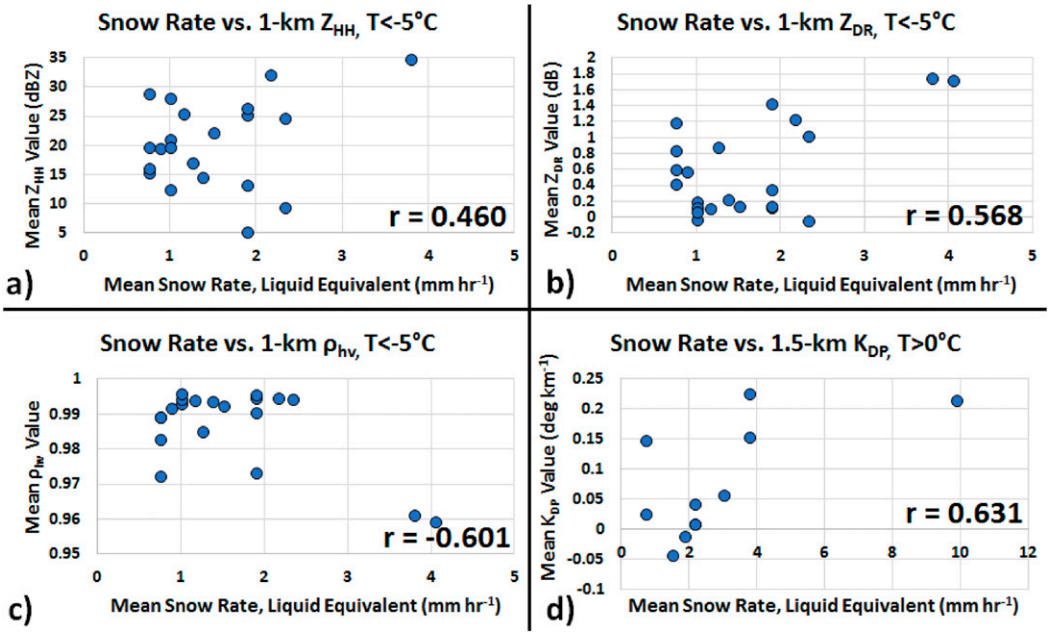

FIG. 7. (a)–(c) As in Figs. 6a–c, but for snow rate at temperature ≤ -5°C. (d) The K_{DP} values at 1.5 km altitude for all data points with temperature > 0°C.

significantly higher) when SN rates were high. These findings suggest possible operational utility in real-time SN rate estimation, but a larger study will be required to confirm these preliminary results.

6. Polarimetric radar observations of elevated convection

As noted previously, the environment above the shallow cold layer was characterized by a veering wind profile and elevated instability (e.g., Fig. 3a). Numerous convective storms occurred across eastern Oklahoma and western Arkansas through the day on 2 March 2014. They produced hail ahead of the cold front (e.g., NWS 2014b), and hail reports were received from an elevated storm behind the cold front in eastern Oklahoma where the surface temperature was <0°C. Given the importance of elevated convection to precipitation rate in this winter storm, polarimetric signatures of the most intense convective cells are presented. Strong elevated convective cells were especially prevalent across east-central Oklahoma from 2000 to 2100 UTC 2 March 2014, and within a convective band south and southwest of KINX from ~1600 to 1730 UTC 2 March.

Two isolated convective cells across east-central Oklahoma exhibited updraft rotation during 2000–2100 UTC 2 March (denoted storms A and B). Maximum velocity difference only briefly exceeded the 30 m s^{-1} threshold established for the mesocyclone detection algorithm (MDA) by Stumpf et al. (1998) for storms within 100 km of a WSR-88D (Fig. 8a), but even if this threshold was not consistently met, persistent rotation appeared to contribute to the longevity and intensity of these convective cells. Thus, the presence of rotation was an important marker of storms that were likely producing substantial winter precipitation impacts. Even if the MDA does not identify them because of low-velocity differences, their presence can be recognized by operational forecasters (e.g., Fig. 8b) and used as a marker of elevated convection that is likely to persist and produce heavy precipitation. Updraft-associated Z_{DR} maxima were generally well defined in both storms, with the top of the 1-dB Z_{DR} region exceeding 2.5 km ARL through the analysis period for one storm and generally 2.2–2.5 km ARL in the other (Fig. 8a). These cannot be called Z_{DR} columns since they do not generally extend above the ambient 0°C level (~3.2 km; not shown), but were important markers of the most intense convective cells. They likely indicate liquid hydrometeors in the updrafts of the storms; lightning and thunder reported during these storms is consistent with a robust mixed-phase region in their updrafts. The presence of these Z_{DR} maxima was a relatively simple way to quickly find areas of heavy precipitation. Additionally, the storms often contained relatively high Z_{DR} values (>3 dB) at low levels (<1 km ARL; typically the lowest elevation angle), especially along their leading edges near the 20-dBZ Z_{HH} contour (Fig. 9a). The collocation

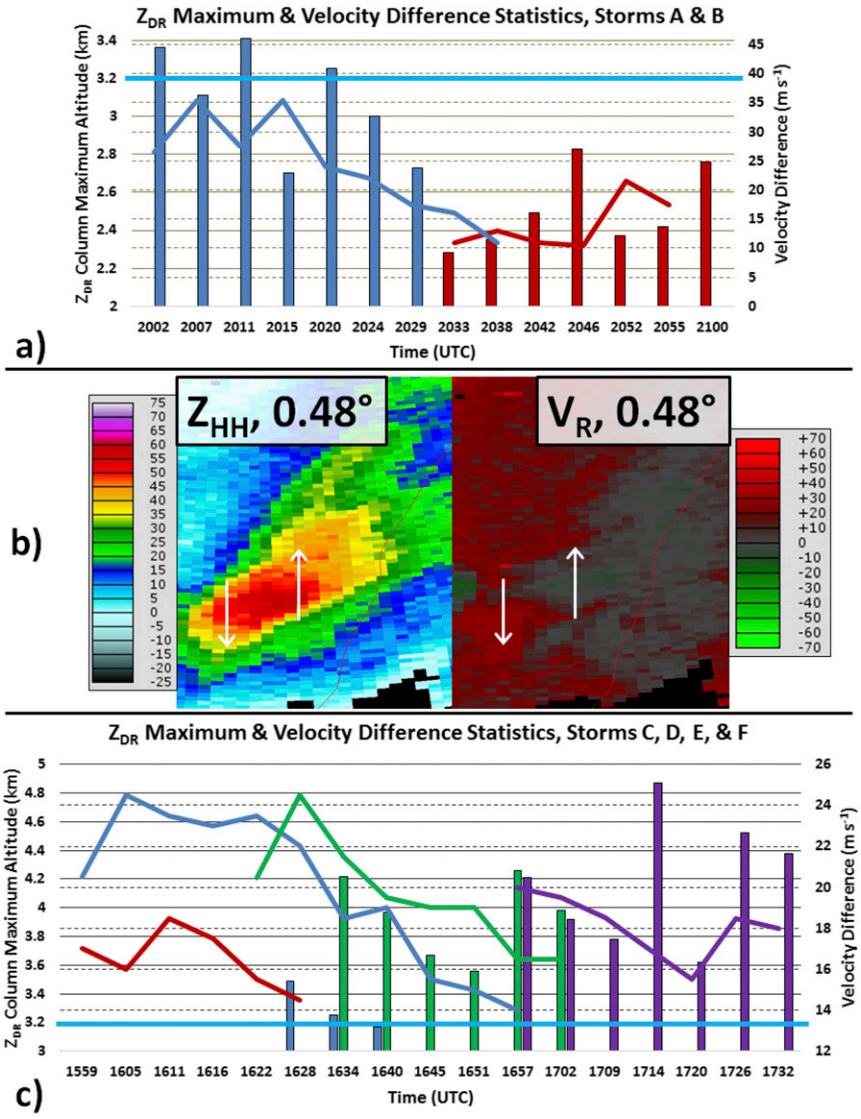

FIG. 8. Maximum altitude of the updraft-associated 1-dB Z_{DR} maximum or column (km; bars) and maximum velocity difference (m s^{-1}; lines) for (a) storms A (blue) and B (red), in the domain of KTLX, and (c) storms C (red), D (blue), E (green), and F (purple), in the domain of KINX. (b) An example of a rotational signature in storm D at 1634 UTC as viewed from KINX (range to storm center ~68.7 km; white arrows indicate sense of rotation). In (a) and (c), quantities are only plotted when available. In each panel, the bars and lines of the same color represent the same storm. Altitude of the Z_{DR} maximum (left axis) is read along the solid gridlines; approximate altitude of the ambient 0°C level (3.2 km) is indicated by the horizontal light blue line. Velocity difference (right axis) is read along the dashed gridlines.

of high-Z_{DR} and relatively low-Z_{HH} values indicates size sorting (e.g., Kumjian and Ryzhkov 2008), and the presence of this signature within the cold air may indicate freezing rain at the surface.

One of the storms in the domain of KTLX (storm B; denoted by red bars and line in Fig. 8a) produced an intense elevated Z_{HH} core. In the 1.79° scan, Z_{HH} values reached 67 dBZ at ~1.88 km ARL (Fig. 9b). The Z_{HH} core was collocated with Z_{DR} values generally from −1 to 0 dB (Fig. 9c) and ρ_{hv} values generally from 0.992 to 0.998 (Fig. 9d). The ambient temperature was ~+7°C at this altitude (estimated from a KMLC RAP sounding; not shown), which was near the center of a layer ~2 km deep with a temperature > 0°C. This signature likely indicates hail or a rain–hail mixture. Social media reports indicated small hail from cells with lower Z_{HH}

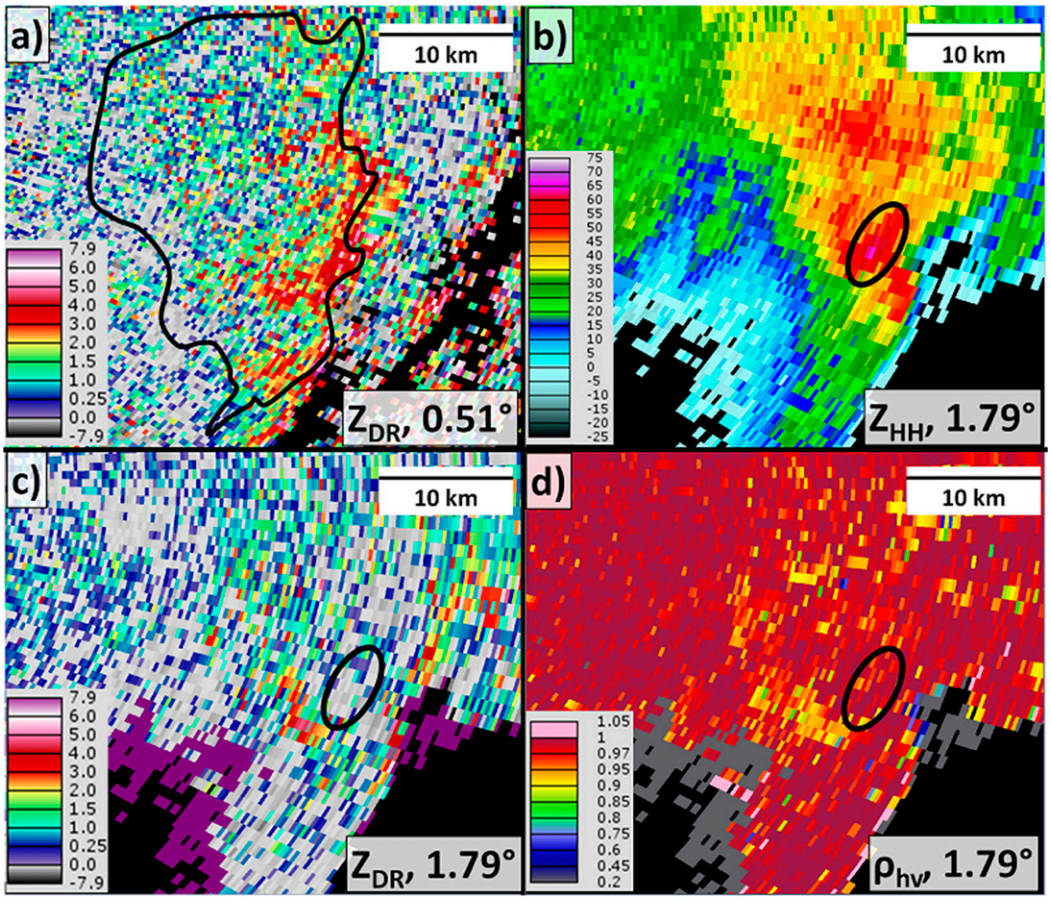

FIG. 9. Polarimetric observations of a storm in the domain of KTLX at 2042 UTC 2 Mar 2014: (a) Z_{DR} (dB) at 0.51° with the 20-dBZ Z_{HH} contour in black, (b) Z_{HH} (dBZ) at 1.79°, (c) Z_{DR} (dB) at 1.79°, and (d) ρ_{hv} at 1.79°. In (b)–(d), the boldface black oval highlights the high-Z_{HH} storm core. Approximate beam centerline altitude to the high-Z_{DR} region on the 20-dBZ contour in (a) is 0.67 km ARL; approximate beam centerline altitude at the center of the ovals in (b)–(d) is 1.88 km ARL. Approximate range to storm core (center of black oval) is 54.1 km.

values to the southwest around the same time. With a surface temperature near −8°C and a subfreezing layer ~950 m (100 hPa) deep, this signature likely indicates IP reaching the surface.

A convective band containing at least four cells with rotating updrafts (e.g., Fig. 8b) was observed from approximately 1600 to 1730 UTC to the southeast of KINX. One storm associated with this band produced a report of 1.9-cm hail over southeast Missouri at 1605 UTC (NCDC 2014), where the surface temperature was near −5°C, though no associated storm reports were received over Oklahoma. The elevated convective environment associated with this band was more favorable for severe storms than is indicated in the sounding shown in Fig. 3a. Though a RAP sounding is not available from the location of the band, a 1600 UTC sounding from the south at KMLC shows 1023 J kg^{-1} of CAPE for a parcel lifted from the top of the inversion, with effective storm-relative helicity of 219 m^2 s^{-2}. At this time, KMLC had a surface temperature of approximately −10°C with a subfreezing depth of ~670 m (not shown). Storms in this elevated band were again characterized by relatively weak rotation not meeting the MDA threshold of Stumpf et al. (1998), though, again, persistent rotation appeared to contribute to storm longevity and intensity (Fig. 8c). Rotation was typically strongest near 1.5 km ARL (just above the inversion top), with typical velocity difference values ~15–22 m s^{-1} (Fig. 8c). The storms were sometimes too far from KINX to reasonably estimate the top of the updraft-associated 1-dB Z_{DR} maximum, which in these storms often extended upward to cold enough temperatures to be considered a Z_{DR} column. When present, Z_{DR} columns extended upward to at least 3.5 km and occasionally to ≥4.5 km ARL (Fig. 8c). Though these storms and those observed by KTLX (described earlier) were not

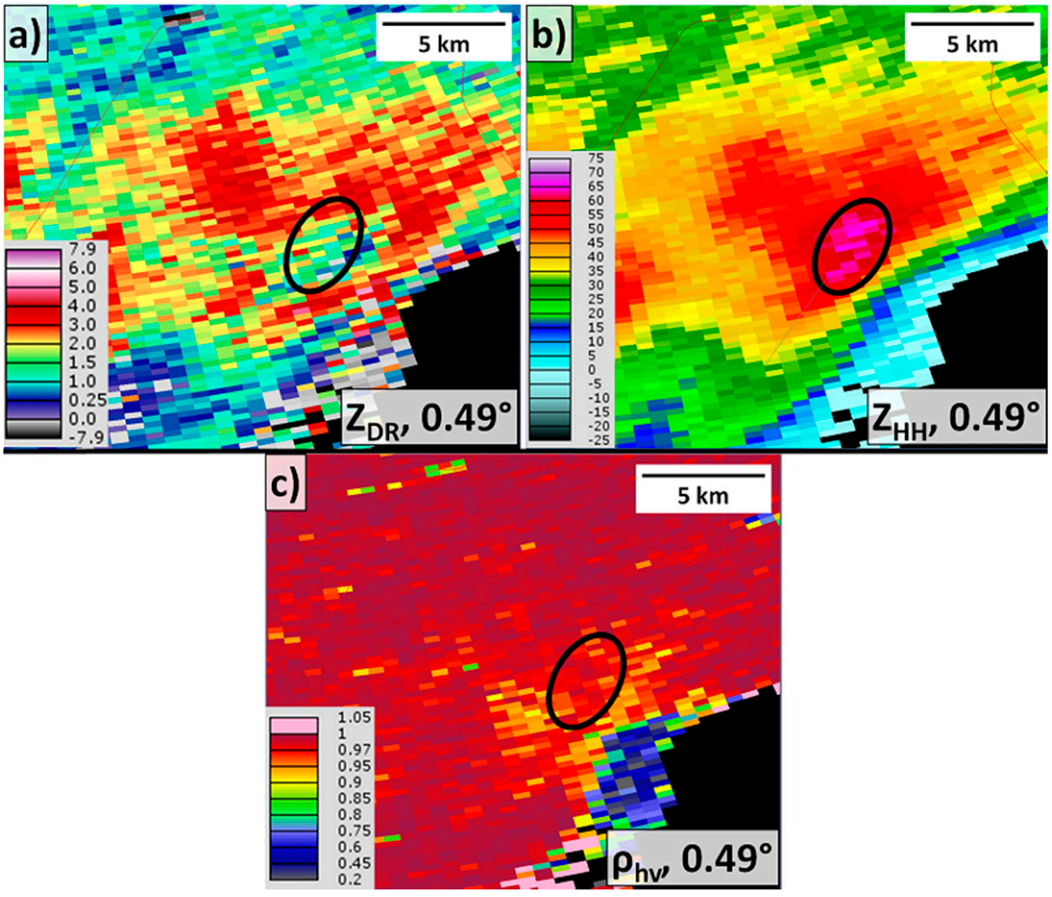

FIG. 10. As in Figs. 9b–d, but for a storm in the domain of KINX at 1726 UTC 2 Mar 2014. Boldface oval denotes the high-Z_{HH} storm core in each panel. Altitude at center of oval is ~0.87 km ARL; range to center of oval is ~67.2 km.

the only rotating storms observed during this winter storm, they were the most prominent and organized.

Storms in the convective band observed by KINX were characterized by high base-scan Z_{DR} values over broad areas (e.g., Fig. 10a), rather than high-Z_{DR} values being confined along the leading edge of storms as observed by KTLX with later storms (cf. Fig. 9a). Again, relatively high Z_{DR} seemed to be a good marker of convective activity and areas likely receiving high precipitation rates including at least some freezing rain. Two storms in the band also contained base-scan Z_{HH} values ≥ 63 dBZ. In both storms, the signature consisted of $Z_{HH} > 63$ dBZ (Fig. 10b) collocated with Z_{DR} of 1–3 dB (Fig. 10a) and ρ_{hv} of 0.955–0.995 (Fig. 10c) at an altitude of ~0.88 km ARL, where the ambient temperature was approximately −7°C (estimated from a nearby RAP sounding; not shown). The temperature above rapidly warmed to 6°–7°C, so falling hydrometeors would encounter rapidly decreasing temperatures in the layer containing the high-Z_{HH} signature. These polarimetric properties point toward a hail–liquid mixture [given high-Z_{HH} values and Z_{DR} occasionally exceeding 2 dB, and ρ_{hv} commonly depressed below 0.97; e.g., Griffin et al. (2014)], which is reasonable given the ambient thermal profile. Hail is also supported by the presence of a three-body scatter signature downrange from the region of high-Z_{HH} values (e.g., Zrnić 1987; Kumjian 2013c; Mahale et al. 2014), visible as a sharp lowering of ρ_{hv} (Fig. 10c).

7. Summary and discussion

Surface precipitation type and intensity were investigated in an early March 2014 winter storm over Oklahoma and Arkansas from a polarimetric radar perspective. In this event, a strong cold front surged southward, leading to the deepening of a shallow but intensely cold air mass. Precipitation began as rain and thunderstorms, then transitioned to mixed freezing rain, ice pellets, and snow. Elevated convection remained present when freezing rain and ice pellets were occurring at the surface, leading to severe-criteria hail well north of the surface 0°C isotherm.

The analysis of a polarimetric hydrometeor refreezing signature in conjunction with mPING reports has several implications for operational forecasting and further research. Numerous and continuous precipitation reports within a region may aid in the analysis of polarimetric radar signatures, and possibly allow the development of algorithms for precipitation-type estimation in real time. Matching surface precipitation reports to QVP signatures has the ability to assess the utility of using QVPs to identify surface precipitation type. In this event, reports of ice pellets closely matched the presence of the refreezing signature, while a lack of reports occurred during a ''break'' in the signature when precipitation was lighter. In further work, environmental conditions responsible for producing these signatures should be examined, along with the reliability of using these signatures to verify surface precipitation type.

Research relating precipitation rate to radar signatures is hampered by the relative scarcity of ground-truth precipitation rate data on short temporal scales. For this winter storm, radar variables had limited utility for the diagnosis of precipitation rate, likely reflecting the temporal scale of precipitation rate data used (up to 20 min) and the long time between successive radar scans (~4–5 min). Nevertheless, rates of FZRA and SN were moderately correlated to values of Z_{HH}, K_{DP}, and sometimes Z_{DR} when segregated by temperature. These preliminary results suggest possible operational utility in low-level values of Z_{HH} and K_{DP} in real-time estimations of FZRA and SN rate. Here, ''low level'' was defined as ~1 km ARL, though the specific altitude could vary in other situations depending on the ambient thermal profile. A freezing rain rate $> 5\,\text{mm}\,\text{h}^{-1}$ was associated with Z_{HH} 3 dBZ higher at 1 km and 4 dBZ higher at 1.5 km compared to periods with lower FZRA rates. The highest snow rates ($>2.25\,\text{mm}\,\text{h}^{-1}$) in this dataset were associated with 1-km Z_{HH} values nearly 5 dBZ higher and 1.5-km Z_{HH} values 14 dBZ higher than periods with lower snow rates. A broad climatological study would be useful to encompass a greater variety of snow rates and include more data points to assess the statistical robustness of these results.

Many winter storms, particularly on the southern Great Plains, contain elevated convective cells that may produce high rates of FZRA and IP when atop a shallow subfreezing near-surface layer. Though these cells may produce highly impactful precipitation (e.g., heavy ice accumulation over a short time period), sparse data are available that would allow a robust radar analysis of the accompanying precipitation rate. Preliminary work presented here shows that a rotating updraft may be present in some of the more persistent storms, which may be an important cue for heavy winter precipitation for operational forecasters. The low-level Z_{DR} field in these elevated storms often contains much higher values than the surroundings, indicating liquid precipitation reaching low levels, and updraft-associated Z_{DR} maxima or columns may be present through a deep layer, suggesting strong updrafts with mixed-phase regions conducive to hail growth and possible electrification. These weakly supercellular storms may be critically important to precipitation-related impacts in some winter storms. Areas of Z_{HH} exceeding 60 dBZ may be present in such elevated convection, and likely are associated with hail. Future work investigating convective microphysics in wintertime scenarios with complex thermal profiles appears warranted.

Acknowledgments. The lead author is supported by NSF Grant AGS-1355916 and an academic appointment at the University of Nebraska—Lincoln. DMT and MRK are funded by NSF Grant AGS-1143948. Jacob Petr is acknowledged for his work on the synoptic background of this event. We thank the anonymous reviewers for their helpful comments.

REFERENCES

Andrić, J., M. R. Kumjian, D. S. Zrnić, J. M. Straka, and V. M. Melnikov, 2013: Polarimetric signatures above the melting layer in winter storms: An observational and modeling study. *J. Appl. Meteor. Climatol.*, **52**, 682–700, doi:10.1175/JAMC-D-12-028.1.

Austin, P. M., and A. C. Bemis, 1950: A quantitative study of the ''bright band'' in radar precipitation echoes. *J. Meteor.*, **7**, 145–151, doi:10.1175/1520-0469(1950)007<0145:AQSOTB>2.0.CO;2.

Bechini, R., L. Baldini, and V. Chandrasekar, 2013: Polarimetric radar observations in the ice region of precipitating clouds at C-band and X-band radar frequencies. *J. Appl. Meteor. Climatol.*, **52**, 1147–1169, doi:10.1175/JAMC-D-12-055.1.

Bernstein, B. C., 2000: Regional and local influences on freezing drizzle, freezing rain, and ice pellet events. *Wea. Forecasting*, **15**, 485–508, doi:10.1175/1520-0434(2000)015<0485:RALIOF>2.0.CO;2.

Brandes, E. A., K. Ikeda, G. Thompson, and M. Schönhuber, 2008: Aggregate terminal velocity/temperature relations. *J. Appl. Meteor. Climatol.*, **47**, 2729–2736, doi:10.1175/2008JAMC1869.1.

Bringi, V. N., and V. Chandrasekar, 2001: *Polarimetric Doppler Weather Radar: Principles and Applications.* Cambridge University Press, 636 pp.

Chen, S., J. J. Gourley, Y. Hong, Q. Cao, N. Carr, P. Kirstetter, J. Zhang, and Z. Flamig, 2016: Using citizen science reports to evaluate estimates of surface precipitation type. *Bull. Amer. Meteor. Soc.*, **97**, 187–193, doi:10.1175/BAMS-D-13-00247.1.

Crowe, C. C., P. Market, B. Pettigrew, C. Melick, and J. Podzimek, 2006: An investigation of thundersnow and deep snow accumulations. *Geophys. Res. Lett.*, **33**, L24812, doi:10.1029/2006GL028214.

Doswell, C. A., III, 1990: Comments on ''A winter mesocyclone over the midwestern United States.'' *Wea. Forecasting*, **5**, 162–165, doi:10.1175/1520-0434(1990)005<0162:COWMOT>2.0.CO;2.

Elmore, K. L., 2011: The NSSL hydrometeor classification algorithm in winter surface precipitation: Evaluation and future development. *Wea. Forecasting*, **26**, 756–765, doi:10.1175/WAF-D-10-05011.1.

——, Z. L. Flamig, V. Lakshmanan, B. T. Kaney, V. Farmer, H. D. Reeves, and L. P. Rothfusz, 2014: mPING: Crowd-sourcing weather reports for research. *Bull. Amer. Meteor. Soc.*, **95**, 1335–1342, doi:10.1175/BAMS-D-13-00014.1.

——, H. M. Grams, D. Apps, and H. D. Reeves, 2015: Verifying forecast precipitation type with mPING. *Wea. Forecasting*, **30**, 656–667, doi:10.1175/WAF-D-14-00068.1.

Giangrande, S. E., J. M. Krause, and A. V. Ryzhkov, 2008: Automatic designation of the melting layer with a polarimetric prototype of the WSR-88D radar. *J. Appl. Meteor. Climatol.*, **47**, 1354–1364, doi:10.1175/2007JAMC1634.1.

Gossard, E. E., R. G. Strauch, D. C. Welsh, and S. Y. Matrosov, 1992: Cloud layers, particle identification, and rain-rate profiles from ZRV_f measurements by clear-air Doppler radars. *J. Atmos. Oceanic Technol.*, **9**, 108–119, doi:10.1175/1520-0426(1992)009<0108:CLPIAR>2.0.CO;2.

Griffin, E. M., T. J. Schuur, A. V. Ryzhkov, H. D. Reeves, and J. C. Picca, 2014: A polarimetric and microphysical investigation of the Northeast blizzard of 8–9 February 2013. *Wea. Forecasting*, **29**, 1271–1294, doi:10.1175/WAF-D-14-00056.1.

Gunn, R., and G. D. Kinzer, 1949: The terminal velocity of fall for water droplets in stagnant air. *J. Meteor.*, **6**, 243–248, doi:10.1175/1520-0469(1949)006<0243:TTVOFF>2.0.CO;2.

Hanesiak, J. M., and R. E. Stewart, 1995: The mesoscale and microscale structure of a severe ice pellet storm. *Mon. Wea. Rev.*, **123**, 3144–3162, doi:10.1175/1520-0493(1995)123<3144:TMAMSO>2.0.CO;2.

Hogan, R. J., P. R. Field, A. J. Illingworth, R. J. Cotton, and T. W. Choularton, 2002: Properties of embedded convection in warm-frontal mixed-phase cloud from aircraft and polarimetric radar. *Quart. J. Roy. Meteor. Soc.*, **128**, 451–476, doi:10.1256/003590002321042054.

Holle, R. L., and A. I. Watson, 1996: Lightning during two central U.S. winter precipitation events. *Wea. Forecasting*, **11** 599–614, doi:10.1175/1520-0434(1996)011<0599:LDTCUW>2.0.CO;2.

Hunter, S. M., S. J. Underwood, R. L. Holle, and T. L. Mote, 2001: Winter lightning and heavy frozen precipitation in the southeast United States. *Wea. Forecasting*, **16**, 478–490, doi:10.1175/1520-0434(2001)016<0478:WLAHFP>2.0.CO;2.

Joss, J., and R. Lee, 1995: The application of radar–gauge comparisons to operational precipitation profile corrections. *J. Appl. Meteor.*, **34**, 2612–2630, doi:10.1175/1520-0450(1995)034<2612:TAORCT>2.0.CO;2.

Keeler, J. M., B. F. Jewett, R. M. Rauber, G. M. McFarquhar, R. M. Rasmussen, L. Xue, C. Liu, and G. Thompson, 2016: Dynamics of cloud-top generating cells in winter cyclones. Part I: Idealized simulations in the context of field observations. *J. Atmos. Sci.*, **73**, 1507–1527, doi:10.1175/JAS-D-15-0126.1.

Kennedy, P. C., and S. A. Rutledge, 2011: S-band dual-polarization radar observations of winter storms. *J. Appl. Meteor. Climatol.*, **50**, 844–858, doi:10.1175/2010JAMC2558.1.

Kumjian, M. R., 2013a: Principles and applications of dual-polarization weather radar. Part I: Description of the polarimetric radar variables. *J. Oper. Meteor.*, **1** (19), 226–242, doi:10.15191/nwajom.2013.0119.

——, 2013b: Principles and applications of dual-polarization weather radar. Part II: Warm- and cold-season applications. *J. Oper. Meteor.*, **1** (20), 243–264, doi:10.15191/nwajom.2013.0120.

——, 2013c: Principles and applications of dual-polarization weather radar. Part III: Artifacts. *J. Oper. Meteor.*, **1** (21), 265–274, doi:10.15191/nwajom.2013.0121.

——, and A. V. Ryzhkov, 2008: Polarimetric signatures in supercell thunderstorms. *J. Appl. Meteor. Climatol.*, **47**, 1940–1961, doi:10.1175/2007JAMC1874.1.

——, and A. D. Schenkman, 2014: The curious case of ice pellets in middle Tennessee on 1 March 2014. *J. Oper. Meteor.*, **2** (17), 209–213, doi:10.15191/nwajom.2014.0217.

——, and W. Deierling, 2015: Analysis of thundersnow storms over northern Colorado. *Wea. Forecasting*, **30**, 1469–1490, doi:10.1175/WAF-D-15-0007.1.

——, A. V. Ryzhkov, H. D. Reeves, and T. J. Schuur, 2013: A dual-polarization signature of hydrometeor refreezing in winter storms. *J. Appl. Meteor. Climatol.*, **52**, 2549–2566, doi:10.1175/JAMC-D-12-0311.1.

——, S. A. Rutledge, R. M. Rasmussen, P. C. Kennedy, and M. Dixon, 2014: High-resolution polarimetric radar observations of snow-generating cells. *J. Appl. Meteor. Climatol.*, **53**, 1636–1658, doi:10.1175/JAMC-D-13-0312.1.

Mahale, V. N., G. Zhang, and M. Xue, 2014: Fuzzy logic classification of S-band polarimetric radar echoes to identify three-body scattering and improve data quality. *J. Appl. Meteor. Climatol.*, **53**, 2017–2033, doi:10.1175/JAMC-D-13-0358.1.

Marshall, J. S., and K. L. S. Gunn, 1952: Measurement of snow parameters by radar. *J. Meteor.*, **9**, 322–327, doi:10.1175/1520-0469(1952)009<0322:MOSPBR>2.0.CO;2.

Martinaitis, S. M., S. B. Cocks, Y. Qi, B. T. Kaney, J. Zhang, and K. Howard, 2015: Understanding winter precipitation impacts on automated gauge observations within a real-time system. *J. Hydrometeor.*, **16**, 2345–2363, doi:10.1175/JHM-D-15-0020.1.

Moisseev, D., S. Lautaportti, J. Tyynela, and S. Lim, 2015: Dual-polarization radar signatures in snowstorms: Role of snowflake aggregation. *J. Geophys. Res. Atmos.*, **120**, 12 644–12 655, doi:10.1002/2015JD023884.

NCDC, 2014: *Storm Data.* Vol. 56, No. 3, 326 pp.

NWS, 2014a: March 1-2, 2014 winter weather event. NWS Forecast Office, Norman, OK. [Available online at http://www.srh.noaa.gov/oun/?n=events-20140301.]

——, 2014b: Winter storm on March 2-3, 2014. NWS Forecast Office, Little Rock, AR. [Available online at http://www.srh.noaa.gov/lzk/?n=win0314yr.htm.]

Picca, J. C., D. M. Schultz, B. A. Colle, S. Ganetis, D. R. Novak, and M. J. Sienkiewicz, 2014: The value of dual-polarization radar in diagnosing the complex microphysical evolution of an intense snowband. *Bull. Amer. Meteor. Soc.*, **95**, 1825–1834, doi:10.1175/BAMS-D-13-00258.1.

Plummer, D. M., G. M. McFarquhar, R. M. Rauber, B. F. Jewett, and D. C. Leon, 2014: Structure and statistical analysis of the microphysical properties of generating cells in the comma head region of continental winter cyclones. *J. Atmos. Sci.*, **71**, 4181–4203, doi:10.1175/JAS-D-14-0100.1.

Prater, E. T., and A. A. Borho, 1992: Doppler radar wind and reflectivity signatures with overrunning and freezing-rain episodes: Preliminary results. *J. Appl. Meteor.*, **31**, 1350–1358, doi:10.1175/1520-0450(1992)031<1350:DRWARS>2.0.CO;2.

Rasmussen, R., and Coauthors, 2012: How well are we measuring snow? The NOAA/FAA/NCAR winter precipitation test bed. *Bull. Amer. Meteor. Soc.*, **93**, 811–829, doi:10.1175/BAMS-D-11-00052.1.

Rauber, R. M., M. K. Ramamurthy, and A. Tokay, 1994: Synoptic and mesoscale structure of a severe freezing rain event: The St. Valentine's Day ice storm. *Wea. Forecasting*, **9**, 183–208, doi:10.1175/1520-0434(1994)009<0183:SAMSOA>2.0.CO;2.

——, L. S. Olthoff, M. K. Ramamurthy, D. Miller, and K. E. Kunkel, 2001: A synoptic weather pattern and sounding-based climatology of freezing precipitation in the United States east of the Rocky Mountains. *J. Appl. Meteor.*, **40**, 1724–1747, doi:10.1175/1520-0450(2001)040<1724:ASWPAS>2.0.CO;2.

Robbins, C. C., and J. V. Cortinas, 2002: Local and synoptic environments associated with freezing rain in the contiguous United States. *Wea. Forecasting*, **17**, 47–65, doi:10.1175/1520-0434(2002)017<0047:LASEAW>2.0.CO;2.

Rosenow, A. A., D. M. Plummer, R. M. Rauber, G. M. McFarquhar, B. F. Jewett, and D. Leon, 2014: Vertical velocity and physical structure of generating cells and convection in the comma head region of continental winter cyclones. *J. Atmos. Sci.*, **71**, 1538–1558, doi:10.1175/JAS-D-13-0249.1.

Rudolph, J. V., K. Friedrich, and U. Germann, 2011: Relationship between radar-estimated precipitation and synoptic weather patterns in the European Alps. *J. Appl. Meteor. Climatol.*, **50**, 944–957, doi:10.1175/2010JAMC2570.1.

Ryzhkov, A. V., T. J. Schuur, D. W. Burgess, P. L. Heinselman, S. E. Giangrande, and D. S. Zrnić, 2005: The Joint Polarization Experiment: Polarimetric rainfall measurements and hydrometeor classification. *Bull. Amer. Meteor. Soc.*, **86**, 809–824, doi:10.1175/BAMS-86-6-809.

——, P. Zhang, H. D. Reeves, J. Krause, M. R. Kumjian, T. Tschallener, S. Troemel Sr., and C. Simmer, 2016: Quasi-vertical profiles—A new way to look at polarimetric radar data. *J. Atmos. Oceanic Technol.*, **33**, 551–562, doi:10.1175/JTECH-D-15-0020.1.

Schneebeli, M., N. Dawes, M. Lehning, and A. Berne, 2013: High-resolution vertical profiles of X-band polarimetric radar observables during snowfall in the Swiss Alps. *J. Appl. Meteor. Climatol.*, **52**, 378–394, doi:10.1175/JAMC-D-12-015.1.

Schrom, R. S., M. R. Kumjian, and Y. Lu, 2015: Polarimetric radar signatures of dendritic growth zones within Colorado winter storms. *J. Appl. Meteor. Climatol.*, **54**, 2365–2388, doi:10.1175/JAMC-D-15-0004.1.

Schuur, T. J., H. Park, A. V. Ryzhkov, and H. D. Reeves, 2012: Classification of precipitation types during transitional winter weather using the RUC model and polarimetric radar retrievals. *J. Appl. Meteor. Climatol.*, **51**, 763–779, doi:10.1175/JAMC-D-11-091.1.

Stumpf, G. J., A. Witt, E. D. Mitchell, P. L. Spencer, J. T. Johnson, M. D. Eilts, K. W. Thomas, and D. W. Burgess, 1998: The National Severe Storms Laboratory mesocyclone detection algorithm for the WSR-88D. *Wea. Forecasting*, **13**, 304–326, doi:10.1175/1520-0434(1998)013<0304:TNSSLM>2.0.CO;2.

Thériault, J. M., R. E. Stewart, J. A. Milbrandt, and M. K. Yau, 2006: On the simulation of winter precipitation types. *J. Geophys. Res.*, **111**, D18202, doi:10.1029/2005JD006665.

——, ——, and W. Henson, 2010: On the dependence of winter precipitation types on temperature, precipitation rate, and associated features. *J. Appl. Meteor. Climatol.*, **49**, 1429–1442, doi:10.1175/2010JAMC2321.1.

——, R. Rasmussen, K. Ikeda, and S. Landolt, 2012: Dependence of snow gauge collection efficiency on snowflake characteristics. *J. Appl. Meteor. Climatol.*, **51**, 745–762, doi:10.1175/JAMC-D-11-0116.1.

Thorp, J. M., and B. C. Scott, 1982: Preliminary calculations of average storm duration and seasonal precipitation rates for the northeast sector of the United States. *Atmos. Environ.*, **16**, 1763–1774, doi:10.1016/0004-6981(82)90269-4.

Trapp, R. J., D. M. Schultz, A. V. Ryzhkov, and R. L. Holle, 2001: Multiscale structure and evolution of an Oklahoma winter precipitation event. *Mon. Wea. Rev.*, **129**, 486–501, doi:10.1175/1520-0493(2001)129<0486:MSAEOA>2.0.CO;2.

Zerr, R. J., 1997: Freezing rain: An observational and theoretical study. *J. Appl. Meteor.*, **36**, 1647–1661, doi:10.1175/1520-0450(1997)036<1647:FRAOAT>2.0.CO;2.

Zrnić, D. S., 1987: Three-body scattering produces precipitation signature of special diagnostic value. *Radio Sci.*, **22**, 76–86, doi:10.1029/RS022i001p00076.

——, and A. V. Ryzhkov, 1999: Polarimetry for weather surveillance radars. *Bull. Amer. Meteor. Soc.*, **80**, 389–406, doi:10.1175/1520-0477(1999)080<0389:PFWSR>2.0.CO;2.

——, R. Raghavan, and V. Chandrasekar, 1994: Observations of copolar correlation coefficient through a bright band at vertical incidence. *J. Appl. Meteor.*, **33**, 45–52, doi:10.1175/1520-0450(1994)033<0045:OOCCCT>2.0.CO;2.